Journal of ELECTRONIC MATERIALS, Vol. 50, No. 3, 2021
https://doi.org/10.1007/s11664-020-08456-5
© 2020 The Minerals, Metals & Materials Society

TMS2020 MICROELECTRONIC PACKAGING, INTERCONNECT, AND PB-FREE SOLDER

Impact of Cryogenic Temperature Environment on Single Solder Joint Mechanical Shear Stability

ANDE KITAMURA,[1] TIMOTHY MATTHEWS,[1] RUBEN CONTRERAS,[1] DAVID ROUTLEDGE,[2] and TAE-KYU LEE [1,3]

1.—Department of Mechanical and Materials Engineering, Portland State University, Portland, OR, USA. 2.—Nordson Dage, Aylesbury, UK. 3.—e-mail: taeklee@pdx.edu

Although the performance of electronic devices in extreme temperature ranges has been extensively studied, the interconnections, which are still mainly Sn-based materials, require thorough observation and assessment to support the mechanical and electrical stability in subzero to cryogenic temperature environments. An in-depth assessment is required because of the nature of Sn, which has a ductile-to-brittle transition temperature of approximately −60°C. Sn-1Ag-0.5Cu (wt.%) (SAC105) solder joints were subjected to shear testing at room temperature and at −196°C at liquid nitrogen temperature. Isothermal aging at 150°C for 50–500 h prior to cryogenic temperature testing indicated further degradation under certain aging conditions. The study presented here investigates the maximum shear strength variations for SAC105 single solder joints with NiAu and Cu-organic solderability preservative (Cu-OSP) pad surface finishes using a multibond tester with a 10-μm shear height and 100-μm/s shear speed. An increase in the maximum shear strength was observed at liquid nitrogen temperature compared to that at room temperature due to an increase in the yield strength and loss in ductility of the solder material in response to the low-temperature environment. The maximum shear strength decreased with isothermal aging due to the crack propagation path variation. Fracture locations were identified between the Ni pad and the $(Cu, Ni)_6Sn_5$ interface for the NiAu surface finish components, and Cu-OSP surface finish solder joints revealed transgranular crack through the Cu_6Sn_5 and crack propagation between the Cu_6Sn_5 and the solder interface. The shift in the full fracture location is discussed in association with electron backscatter diffraction (EBSD) analysis on partially sheared solder joints at room temperature and at −196°C.

Key words: Cryogenic temperature, solder, solder shear, microstructure, interconnect

INTRODUCTION

Recent deep-space exploration, quantum computing, and extreme environmental conditions have pushed the limits of interconnect reliability challenges in electronic devices to cryogenic temperatures. Aerospace exploration has the potential to encounter planets and moons with cryogenic temperatures of approximately −220°C, while quantum computing requires an environment of cryogenic temperatures of approximately − 270°C.[1–3] Even though the solder joints and interconnects might not be exposed directly to these temperatures, the mechanical and electrical stability at subzero temperatures are of great interest, and

(Received June 17, 2020; accepted August 27, 2020; published online September 15, 2020)

understanding the mechanical properties of solder interconnects at cryogenic temperatures is important to improve their reliability in such harsh conditions. An interconnect inside an electronic device is constructed with either Cu or Ni layers that have face-centered cubic (FCC) lattice crystal structures, unlike the Sn-based solder joint, which has a body-centered tetragonal (BCT) crystal structure. FCC lattice structure materials in general do not experience ductile-to-brittle temperature transitions, but Sn shows brittle behavior at low temperatures, which could lead to a high failure risk due to fast crack propagation.[4–7] Several studies, including the work by An et al., investigated the failure mode and fracture mechanism of several types of Sn-based solders at a temperature range of 20°C to −150°C using a Charpy test and found that for pure Sn, a brittle fracture occurs below −60°C with both transgranular and intergranular fracture modes. It was also indicated that the addition of Cu in the SAC305 alloy altered the fracture toughness, shifting the ductile-to-brittle transition temperature to a higher temperature between −30°C and −40°C.[6,7] However, along with the ductile-to-brittle transition temperature in Sn, the mechanical response of the Sn-based solder joint at low temperatures presents other important behavior shifts. The interconnect mechanical shock performance is closely related to the level of shock absorption. If a solder joint can absorb a certain amount of shock-induced strain, the weak interface experiences a decreased amount of damage and results in an increased life cycle number at a given shock condition. Previous studies show that low-Ag solder joints and fast-cooling-rate solders have an increased shock performance due to their accelerated grain refinement and grain recrystallization behavior, which ultimately are very sensitive to absorbing shock-induced strain.[8,9] Additionally, solder joints in the elevated temperature shock test show an enhanced shock performance due to the low yield strength at high temperatures, which results in an increased degree of ductile behavior during dynamic shock.[10] Shock performance in subzero temperature environments is expected to show a very different behavior since the solder joints are expected to have a decreased potential strain absorption capability due to their increased yield strength and ductile-to-brittle transition-induced behavior. The Sn solder joint itself may avoid damage accumulation, but the localized interface has an increased strain and stress to accommodate. The change in fracture toughness of solder alloys due to temperature and the correlation to fracture surface modes of SAC305 solder in temperatures ranging from −196°C to 25°C were studied by Tian et al.,[11] which revealed that the fracture surface shifted from ductile fracture to brittle fracture along with a change in fracture location from the bulk solder to the solder to the intermetallic layer interface with a decrease in the temperature. Due to this important phenomenon, in recent years, careful and systematic studies have been actively published focused on both the Sn bulk property and solder joint configuration at relatively high strain rates to mimic the shock condition.[6,7,11,12] However, fracture at the interface may have a high possibility of occurring even at slow strain rates since the absorption of the strain is constrained at subzero to cryogenic temperatures. Thus, great interest still remains in interconnect mechanical stability in actual solder joint structures with small grain sizes, identical solder interconnect geometries, metallization and especially slow strain rates at cryogenic temperatures. In this study, maximum shear strength measurements for SAC105 single solder joints attached on both NiAu and Cu-organic solderability preservative (OSP) pad surface finishes at room temperature and liquid nitrogen temperature (−196°C) were conducted using a multibond tester (Nordson DAGE 4000Plus) with a relatively slow shear speed. The mechanical properties were investigated along with the fracture mechanics and microstructure of SAC105 solder joints with cryogenic shear testing.

EXPERIMENTAL PROCEDURES

The sample used in this study is shown in Fig. 1. A body size of 12 × 12 mm comprising fine-pitch ball grid array (BGA) components with two different surface finishes, an electrolytic NiAu surface finish and a copper pad organic surface preservative (Cu-OSP) surface finish, and one type of solder alloy, Sn-1.0Ag-0.5Cu (wt.%) (SAC105), were used. The BGA components had 300-μm-diameter solder balls in an arrangement with a 0.5-mm pitch. As indicated in Fig. 1a, the second rows from the edge solder array were removed to provide clearance for solder ball shearing of the first row. The shear applied solder ball location (red circle) and the shear direction (white arrow) are indicated in Fig. 1a. Two sides of the first-row solder balls along the edge were sheared by rotating the sample 180° after finishing the edge on one side so that the shear direction was always from the edge toward the component center. Figure 1b and c shows the solder joint configuration and schematic shear tool configuration with dimensions for both the electrolytic NiAu and Cu-OSP surface finishes. The width of the shear tool was 400 μm, and all shear tests were performed with a shear height of 10 μm and shear speed of 100 μm/s. The shear height was selected based on expanded shear testing with various shear heights. The 10-μm shear height was determined by comparing differing shear heights, and it was found that 10 μm was the optimal shear height to analyze the effect of the intermetallic growth and the effect it had on crack propagation near the substrate and solder joint interface. The general industry recommendation for shear height ranges from 10 to 15% of the solder

diameter, but with ~ 10% of the solder height, the mechanical behavior response comes from a region that is slightly away from the interface. Since the behavior near the interface is important in this study, the 10-μm shear height was selected. The cooling stage apparatus for the −196°C cryogenic temperature shear condition is shown schematically in Fig. 2. The BGA component is mechanically clamped inside an aluminum container stage, then submerged into liquid nitrogen for 10 s before contact with the also-submerged shear tool for temperature saturation of both the solder joint and shear tool. The liquid nitrogen immersion testing methodology was selected to achieve an isothermal temperature condition throughout the sample configuration with multiple layers of materials. The combination of epoxy, glass fiber and metal layers significantly induced a thermal gradient if the heating/cooling source is unidirectional. Full immersion into liquid nitrogen provided a solution to this, since all sample layers, including the shear tool, maintained an isothermal temperature condition during testing. A thermocouple was attached to the location indicated in Fig. 2b to ensure a consistent solder joint temperature before initiating each shear test. To compare the interface microstructure variation, samples were isothermally aged at 150°C for 50 h, 100 h and 500 h before shear testing. For microstructure analysis, cross sections of the samples were observed using scanning electron microscopy (SEM, FEI Sirion XL30) equipped with an electron backscatter diffraction (EBSD) detector (Oxford Instruments) to analyze the crack propagation path, fracture surface and localized strain and stress via strain contour and grain reference orientation deviation (GROD) maps.

RESULTS AND DISCUSSION

Figure 3 shows the room-temperature shear test data per surface finish and isothermal aging preconditions. Selected shear load-to-distance curves for the NiAu surface finish that were selected from each isothermal aging condition are plotted in Fig. 3a, and the maximum shear load values per condition are plotted in Fig. 3c. During room-temperature shearing, the solder joints were easily able to plastically deform, and all of the sheared surface indicated ductile deformation, as shown in the inset figure in Fig. 3a. Overall, the maximum shear load was in the 260-g to 330-g range with a small but identifiable difference between the isothermal aging conditions, and a downward trend associated with an increasing aging time at 150°C was observed. The shear test results for the Cu-OSP samples are shown in Fig. 3b and d and can be compared to those for the samples with a NiAu surface finish. The maximum shear load with no aging was similar to that of the samples with a NiAu surface finish, but revealed an upward trend with increasing aging times, which is the opposite trend to that of the

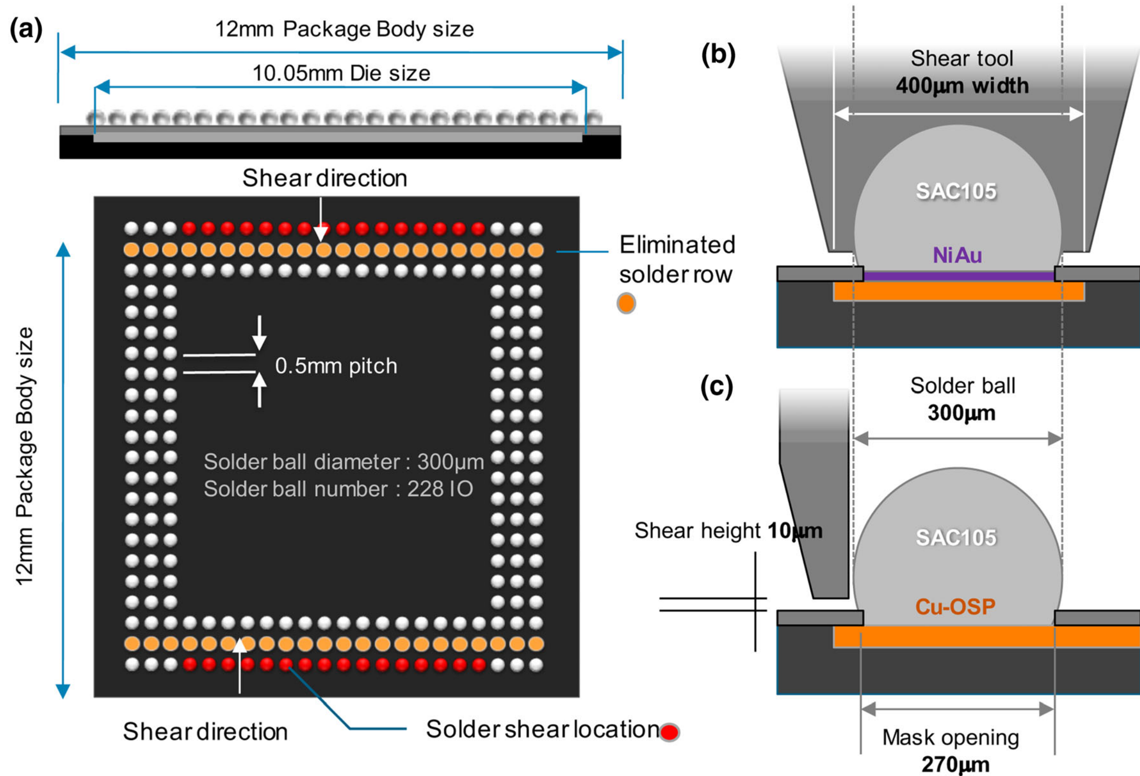

Fig. 1. Ball grid array (BGA) test component configuration. (a) Solder joint arrangement top-down view, (b) NiAu surface finish solder joint configuration and shear tool dimension front view and (c) Cu-OSP surface finish solder joint configuration side view.

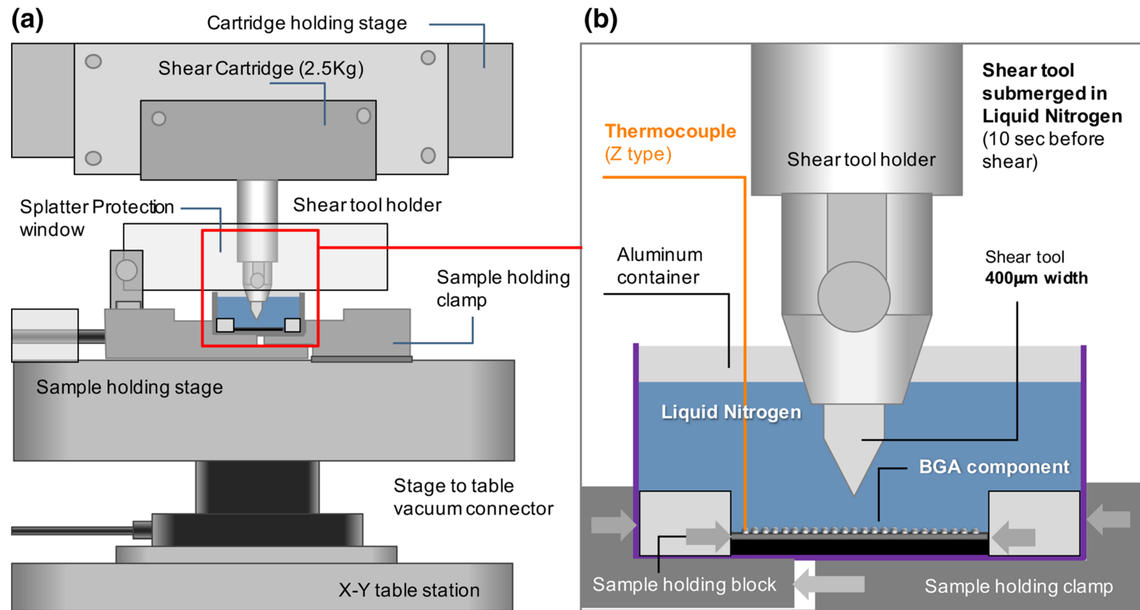

Fig. 2. Schematic of the liquid nitrogen shear test apparatus. (a) Apparatus with the LN_2 holding container (Dage 4000Plus) and (b) close-up view of the LN_2 sample holder with the BGA sample for the test at $-196°C$.

samples with a NiAu surface finish. One of the reasons for this upward trend with increasing aging time for Cu-OSP can be explained by the higher Cu concentration near the interface with long aging times. An earlier study by Duh et al. on the Cu concentration with different surface finishes identified that a higher Cu concentration resulted in high-reliability performance.[13] Since the 10-μm shear height in this test condition revealed the mechanical response near the interface region rather than in the overall bulk solder joint, the increase in Cu concentration near the interface resulted in an increased shear strength with increasing aging time. Along with the upward trend of the shear load with increasing aging time, the shear load-to-distance curves in Fig. 3b also show a shift in the peak shear load toward an increased distance with increasing aging conditions, which potentially indicates an increased ductility of the near-interface region for the samples with the Cu-OSP surface finish compared to that for the samples with the NiAu surface finish.

The shear test in liquid nitrogen ($-196°C$) for the NiAu and Cu-OSP surface finishes can be seen in Fig. 4. Compared to those for the room-temperature shear test curves in Fig. 3a and b, the shear curves obtained at $-196°C$ in Fig. 4a and b show an abrupt increase in shear load up to 1000 g immediately after the shear tool made contact with the solder joint. Most of the shear curves reached a peak shear load in a travel distance of less than 10 μm. For the samples with a NiAu surface finish, the unaged samples showed the highest maximum shear load values that then decreased with increasing aging time (Fig. 4c). The shear load-to-distance curve shape in Fig. 4a also shows a change with isothermal aging conditions. The shear curves for unaged samples show an increased distance to the peak shear load with a relatively rounded curved peak region, but the shear load curves contained sharp peaks with increasing isothermal aging times. A similar trend is observed for the samples with the Cu-OSP surface finish in Fig. 4b and d, but with a slightly increased maximum shear load per isothermal aging condition and decreased variation in the maximum shear load per isothermal aging time variation. The shear load curve in Fig. 4b also shows a slow decrease in the shear load after the peak shear load compared to that for the samples with a NiAu surface finish in Fig. 4a, which indicates that the solder bulk material remained intact on the fracture surface longer than the samples with a NiAu surface finish. The inset in Fig. 4b shows a top-down SEM image of a solder joint with the Cu-OSP surface finish that was sheared to maximum shear load condition before the solder joint separated from the fracture surface. The exposed fracture surface revealed a brittle fracture mode, which is discussed in detail in Fig. 8.

Figure 5 presents bright-field optical cross sections before and after the shear test in a $-196°C$ temperature environment. In the case of the samples with the NiAu surface finish, during ball attachment reflow, Ni diffused from the substrate side into the solder bulk region, forming $(Cu, Ni)_6Sn_5$ at the solder-to-Ni interface, as shown in Fig. 5a. In a previous publication, the composition analysis showed that the average Ni concentration at the interface was 19.4 at.% in $(Cu, Ni)_6Sn_5$.[14] The composition of $(Cu, Ni)_6Sn_5$ is similar to that of $Cu_4Ni_2Sn_5$, which is the most stable phase at the solder-to-Ni interface.[15] Although it is expected that

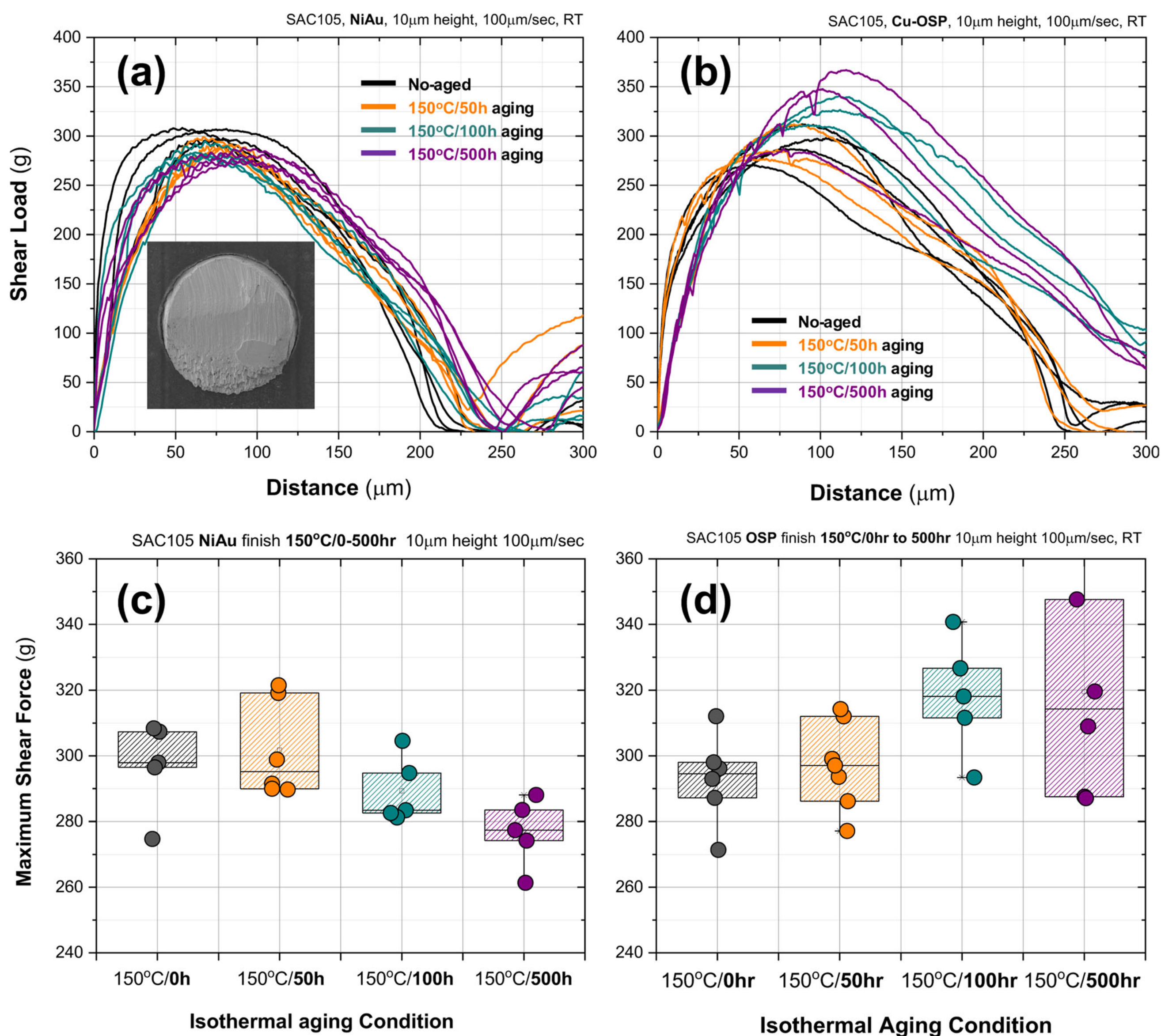

Fig. 3. Room-temperature shear test results. Shear load-to-distance curves for (a) samples with NiAu surface finish and (b) Cu-OSP surface finish with 150°C isothermal aging time variation. (c) Maximum shear load per aging condition for samples with NiAu surface finish and (d) Cu-OSP surface finish from Fig. 3(a) and (b). SEM image of the facture surface is in the inset of Fig. 3(a).

variations arise from any combination of an inhomogeneous distribution of Ni among $(Cu, Ni)_6Sn_5$ in the intermetallic compound (IMC) layer,[16] the intermetallic phase at the Ni substrate to SAC105 solder is presented as $(Cu, Ni)_6Sn_5$ in this paper, since no detailed analysis was performed to identify the accurate Ni concentration. After aging at 150°C for 500 h, the intermetallic layer increased in thickness at the interface, as shown in Fig. 5c. For the fracture location in the NiAu surface finish samples, Fig. 5d–f reveals that the fracture occurred at the interface between the Ni pad and the $(Cu, Ni)_6Sn_5$ intermetallic layer as the main crack propagation path for the shear samples tested at −196°C. The optical cross-sectional images for the unaged, 150°C/50 h, and 150°C/500 h aged samples showed identical full fracture locations in Fig. 5d, e and f, respectively. The associated SEM fracture surface images for the samples with the NiAu surface finish after shearing at −196°C are shown in Fig. 6. As shown in Fig. 6a, the unaged then −196°C sheared surface contained a small localized region comprising a mixture of $(Cu, Ni)_6Sn_5$ and residual Sn with a majority of the fracture surface area revealing the Ni pad. High-magnification SEM and energy-dispersive X-ray spectroscopy (EDS) images from the white box (region A) are shown in Fig. 7, which identified the $(Cu, Ni)_6Sn_5$ and residual Sn mixed region indicated in Fig. 6a along with the exposed Ni pad surface region in Fig. 6e (region B). The associated SEM image and EDS map in Fig. 7b indicate a

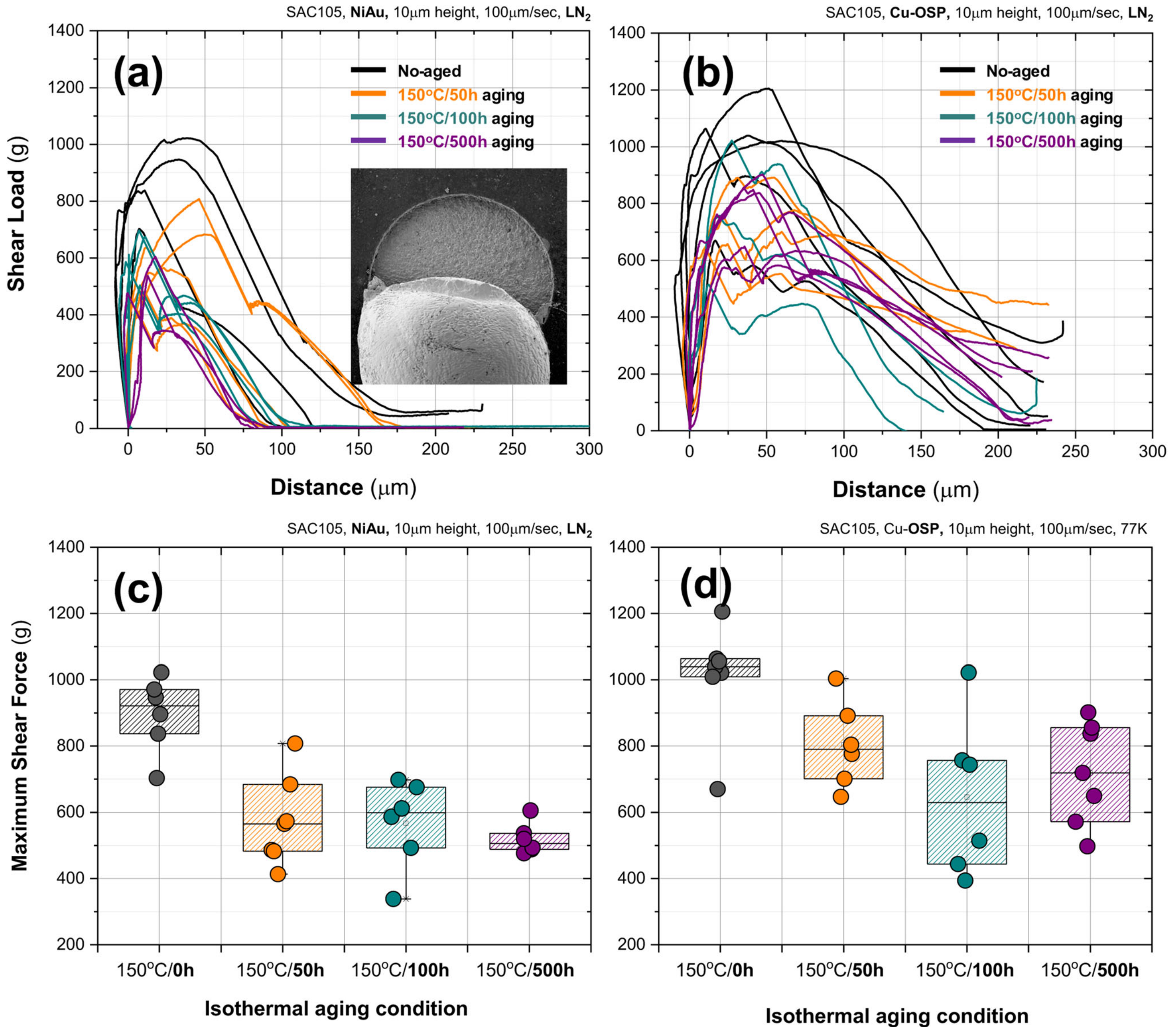

Fig. 4. Shear test results at liquid nitrogen temperature (−196°C). Shear load-to-distance curves for samples with (a) NiAu surface finish and (b) Cu-OSP surface finish with 150°C isothermal aging time variation. Maximum shear load per aging condition from Fig. 4(a) and (b) for samples with (c) NiAu surface finish and (d) Cu-OSP surface finish. SEM image of the fracture surface is in the inset in Fig. 4(a).

region comprising a mixture of (Cu, Ni)$_6$Sn$_5$ and residual Sn and a predominance of Ni, which is from the area in Fig. 6a (region A). The increased maximum shear load values obtained at −196°C from the unaged samples shown in Fig. 4a and c can be explained by these existing localized (Cu, Ni)$_6$Sn$_5$ and residual Sn mixed regions, which potentially decelerate the crack propagation rate during shear testing at −196°C and result in an increased shear load during full crack propagation. The 150°C/50 h isothermally aged sample also showed a small region of (Cu, Ni)$_6$Sn$_5$ indicated by the white arrow in Fig. 6b, but with longer aging times of 150°C/100 h and 150°C/500 h, the samples showed no significant indication of (Cu, Ni)$_6$Sn$_5$ or residual Sn at the fracture surface.

Compared to that for the solder joint samples with the NiAu surface finish, the Cu-OSP surface finish samples showed a crack propagation path in the Cu$_6$Sn$_5$ layer with transgranular and intergranular fracture modes. The optical cross sections in Fig. 5g, h and i show the Cu-OSP–SAC105 interface before shear testing with no aging, 150°C/50 h and 150°C/500 h aging, respectively. Along with an increase in the Cu$_6$Sn$_5$ thickness, an increase in the Cu$_3$Sn layer is also observed. In Fig. 5j, the full fracture occurred near the root of the Cu$_6$Sn$_5$ intermetallic layer and at the interface between the Cu pad and the Cu$_6$Sn$_5$ layer. The associated fracture surfaces in Fig. 8a and e revealed a mixture of Cu$_6$Sn$_5$ transgranular cracks and fractures between the Cu pad and Cu$_6$Sn$_5$. There were also localized areas that show that residual Sn remained attached to the

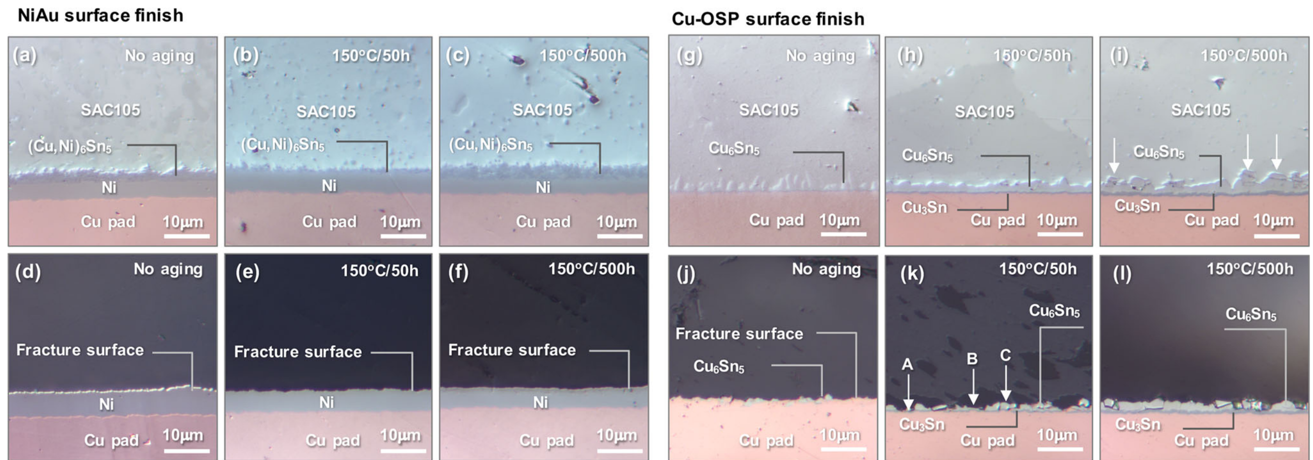

Fig. 5. Optical bright-field cross-sectional images before and after the shear test in a −196°C temperature environment. Initial microstructure per isothermal aging for samples with a (a)–(c) NiAu surface finish and a (g)–(i) Cu-OSP surface finish. Samples with (d)–(f) NiAu surface finish and (j)–(l) Cu-OSP surface finish after the −196°C shear test. Arrows in (i) indicate the Cu_6Sn_5 grains with horizontal cracks inside.

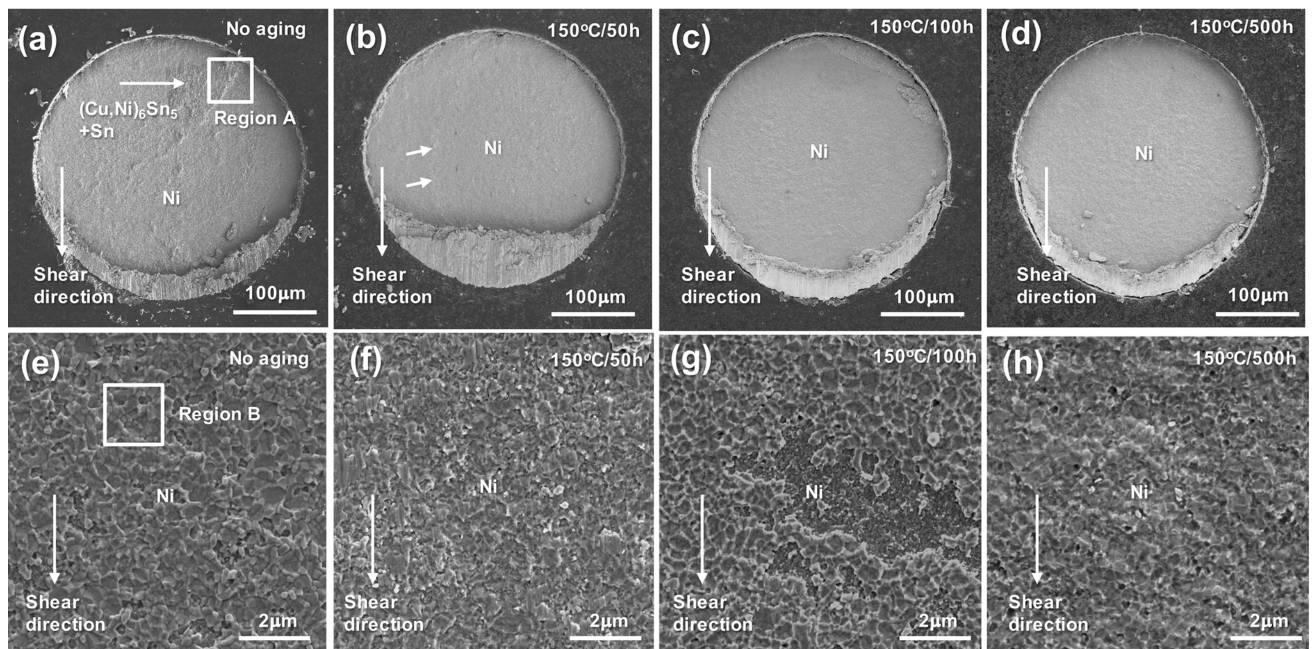

Fig. 6. Scanning electron microscopy images of the fracture surface in the solder joint with the NiAu surface finish after shear testing in a −196°C temperature environment with the isothermal aging condition. (a), (e) Shear test after no aging; (b), (f) shear test after 150°C/50 h aging; (c), (g) shear test after 150°C/100 h aging; and (d), (h) shear test after 150°C/500 h aging. (e), (f), (g) and (h) High-magnification SEM images from the midsection of each aging condition fracture surface. The arrows in (a) and (b) indicate the (Cu, $Ni)_6Sn_5$ and residual Sn mixed region.

top of the Cu_6Sn_5 intermetallic grains. As indicated in Fig. 8e with the letter "T," the unaged samples shear tested at −196°C showed relatively large areas identified as transgranular fractures, where cracks propagated through each Cu_6Sn_5 intermetallic grain. Compared to that for the unaged samples, upon aging with a 150°C/50 h isothermal anneal, the Cu_3Sn layer began to stabilize, as shown in Fig. 5h and k, and a more uniform Cu_6Sn_5 grain distribution was observed in the fracture surface after the −196°C shear test, as shown in Fig. 8b and g. Several crack paths were observed, as indicated in Fig. 5k: between the Cu_3Sn and Cu_6Sn_5 (marked with arrow *A*), transgranular fracture inside the Cu_6Sn_5 (marked with arrow B) and fracture between the top of the Cu_6Sn_5 grains and Sn bulk solder interface (marked with arrow *C*). The associated SEM fracture surface images are shown in Fig. 8b and f. A decreased amount of residual Sn was observed on the fracture surface with a mixture of transgranular fracture and fracture between the top of the Cu_6Sn_5 grains and the Sn interface. The region indicated with a white arrow (*D*) shows that the Cu pad surface was revealed with a Cu_3Sn

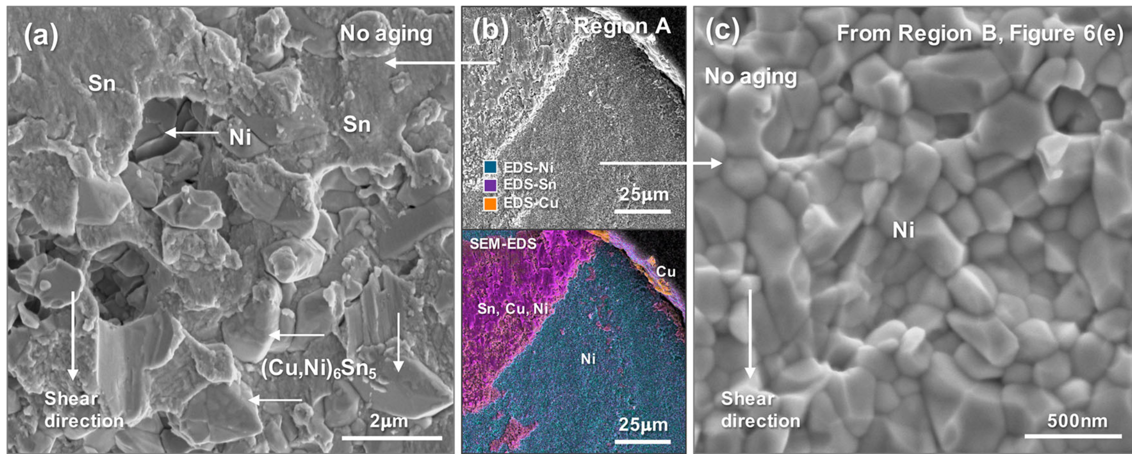

Fig. 7. High-magnification scanning electron microscopy images of the fracture surface after solder joint shear test in the −196°C temperature environment for the sample with the NiAu surface finish from Fig. 6(a) and (e). (a) (Cu, Ni)$_6$Sn$_5$ and residual Sn mixture region from indicated region A in Fig. 6(a), (b) SEM-EDS map with the scanned area indicated in Fig. 6(a) as region A, and (c) high-magnification SEM images from region B in Fig. 6(e). Figure 7(a) and (c) have different magnifications and scales.

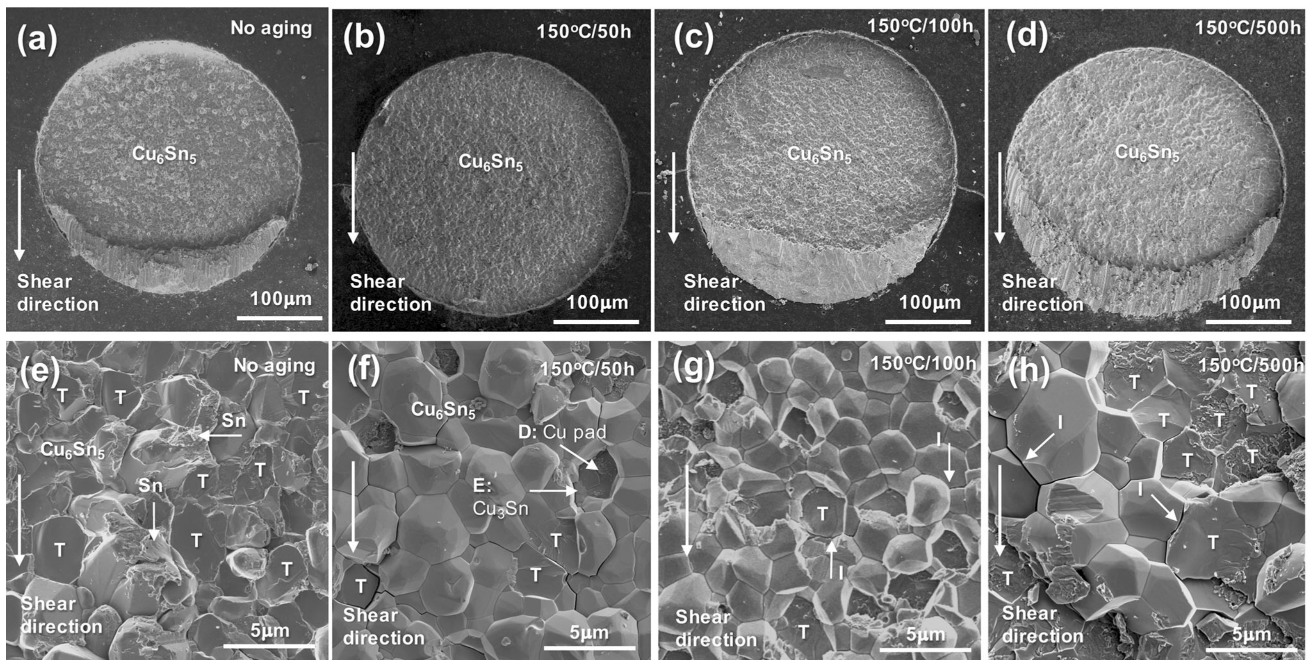

Fig. 8. Solder joint fracture for sample with Cu-OSP surface finish observed with surface scanning electron microscopy after the shear test in a −196°C temperature environment per isothermal aging condition. (a), (e) Shear test after no aging, (b), (f) shear test after 150°C/50 h aging, (c), (g) shear test after 150°C/100 h aging, and (d), (h) shear test after 150°C/500 h aging. (e), (f), (g) and (h) are high-magnification SEM images from the midsection of each aging condition fracture surface. Regions indicated with "T" are transgranular crack locations through Cu$_6$Sn$_5$ grains, and "I" indicates intergranular crack locations between Cu$_6$Sn$_5$ grains.

region at the edge of the open separation, which is also indicated with an arrow (E). With continued isothermal aging, the observed fracture propagation paths were similar and revealed large Cu$_6$Sn$_5$ grain sizes with increasing aging times, as shown in Fig. 8g and h, sheared after aging at 150°C/100 h and 150°C/500 h, respectively. Crack propagation paths were observed at interfaces either between the Cu$_6$Sn$_5$ and bulk Sn or transgranular fracture inside Cu$_6$Sn$_5$. Compared to those for the unaged and 150°C/50 h aged samples, the 150°C/100 h and 150°C/500 h aged samples also revealed vertical intergranular fracture locations between the Cu$_6$Sn$_5$ grains, as indicated by the white arrows (I) in Fig. 8g and h. Even though the overall crack propagation paths in Cu-OSP samples were similar between the unaged and isothermally aged samples, a small variation in the maximum shear load per isothermal aging condition existed that can be observed in the maximum shear load distribution

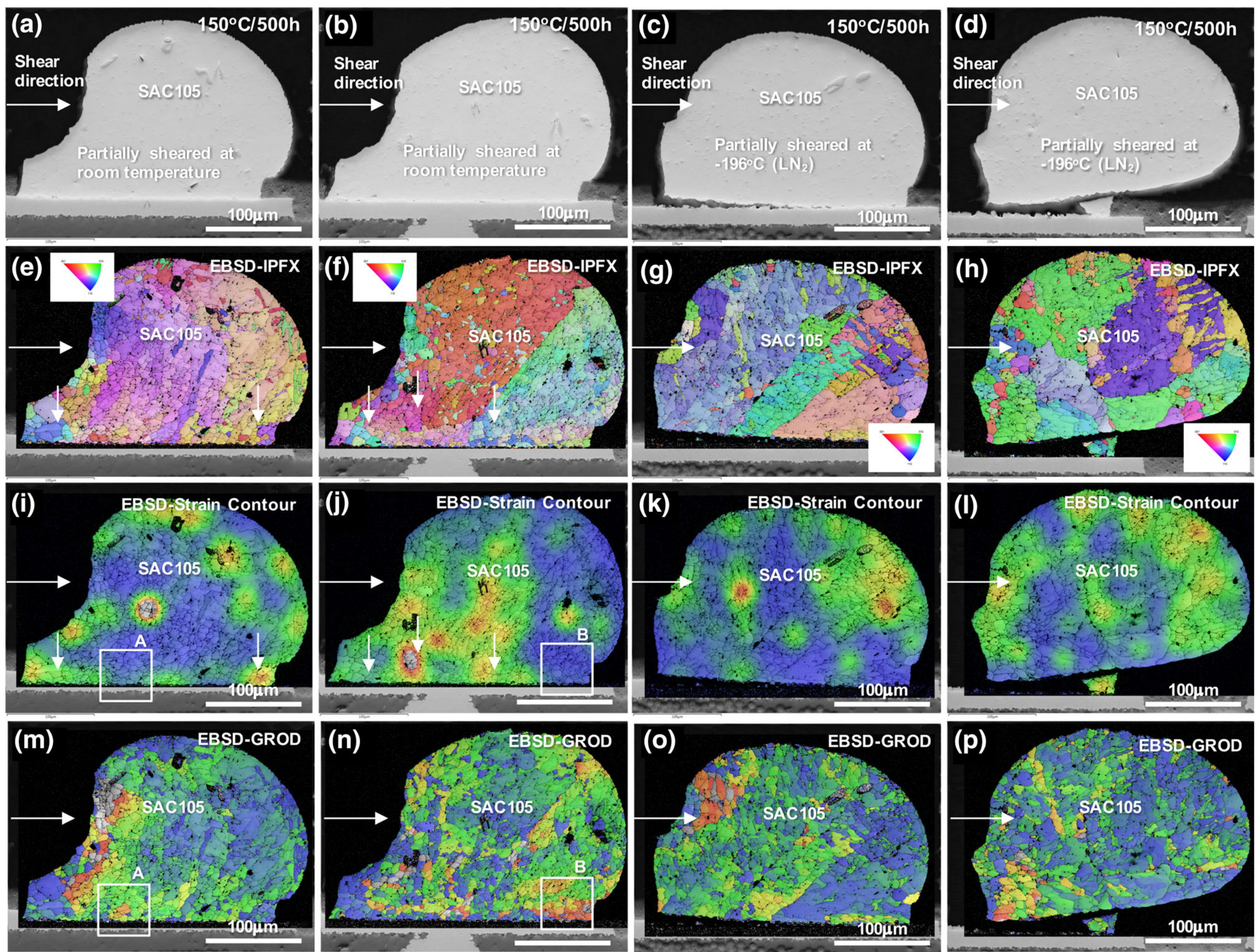

Fig. 9. SEM and EBSD cross-sectional microstructure comparison of partially sheared SAC105 Cu-OSP samples at room temperature (a), (b) and after shearing at −196°C (c), (d). (e)–(h) EBSD inverse pole figure (IPF) images as a function of the shear temperature, (j)–(l) EBSD strain contour map, and (m)–(p) grain reference orientation deviation (GROD) map per solder joint (a)–(d). All sheared solder joints with isothermal aging at 150°C/500 h.

plot shown in Fig. 4b. The increased maximum shear load for the unaged samples can be explained by the main crack path between the Cu pad and Cu_6Sn_5 interface, which had an irregular propagation path and provided obstacles for a fast propagation rate. The 150°C/50 h and 150°C/100 h isothermally aged samples had an identifiable decrease in shear load compared to that for the unaged samples due to the easy crack propagation path, mainly at the interface between the top of the Cu_6Sn_5 and bulk Sn, with a relatively smooth and fast propagation path. However, at the same time, vertical intergranular fracture paths began to form with the 150°C/500 h aging condition that potentially mitigated the fast crack propagation and resulted in a slight increase in the maximum shear load. Additional factors impacting the crack propagation can be seen in Fig. 5i after 150°C/500 h aging. Due to the two different lattice structures for Cu_6Sn_5, namely, monoclinic and hexagonal,[17,18] pre-existing cracks were observed after aging even before shear testing at −196°C, as shown in Fig. 5i indicated by the white arrows. These pre-existing cracks can potentially guide the crack propagation path during cryogenic shearing, as shown at the fracture surface in Fig. 8h, which can accelerate the crack propagation rate. However, given the various factors that can decelerate and accelerate the propagation rate with an increased or decreased maximum shear load, the main crack path during shear testing at −196°C remained at the substrate-to-solder intermetallic layer interface region.

A comparison of the SEM cross section and EBSD results from partially sheared SAC105 Cu-OSP samples at room temperature (Fig. 9a and b) versus liquid nitrogen temperature (−196°C) (Fig. 9c and d) is shown in Fig. 9. The partially sheared samples were used to identify the location of the localized maximum strain and stress region during shear. Shear was applied per solder joint until the load reached 70% of the maximum shear load. The partial solder ball shear in Fig. 9 was applied with

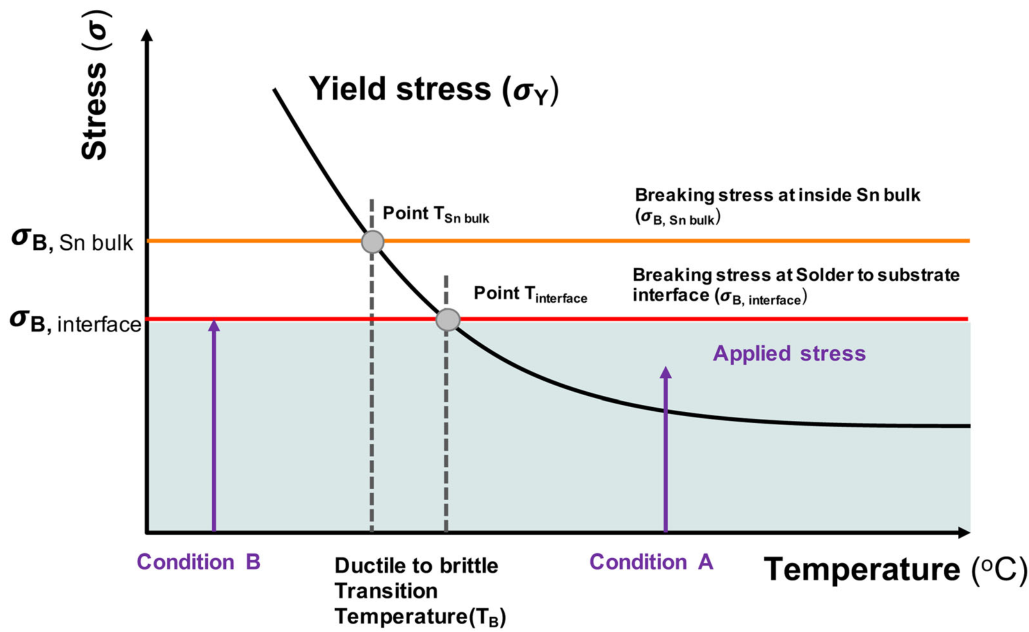

Fig. 10. A schematically described temperature-to-stress correlation Yoffee diagram, which defines the ductile-to-brittle transition temperature.

a shear height of 30 μm. Unlike the data presented for a 10-μm shear height, these partially sheared solder balls were used to compare the temperature effect related to the microstructure evolution. Partial shear test data were not included in the data analysis and were only used for EBSD analysis. As shown in Fig. 9a and b, the SEM cross-sectional images show the plastically deformed region near the shear tool contact to the solder joint during room-temperature shearing. For both solder joints, locally deformed grains were observed in the inverse pole figure (IPF) maps shown in Fig. 9e and f at the shear tool contact region and near the solder-to-substrate interface, as indicated by the white arrows. The associated EBSD strain contour maps in Fig. 9i and j also revealed the plastic deformation region near the solder-to-substrate interface region. Along with the EBSD strain contour map, the grain orientation reference deviation (GROD) map indirectly presents the relative residual stress level compared to the adjacent grains by comparing the level of grain tilting per individual grain versus a grain orientation reference.[19] As shown in Fig. 9m and n, an increased level of residual stress regions are indicated in the GROD map along the solder-to-substrate interface, which was not yet affected by the shear tool-induced plastic deformation (indicated with boxes A and B in Fig. 9i, m and j, n, respectively). Compared to that for the room-temperature shearing, the shear tool contact region for partial shearing at -196°C shown in Fig. 9c and d did not induce a high-intensity localized region of plastic deformation and showed a limited accumulation of plastic deformation, as indicated by the EBSD strain and GROD map in Fig. 9k, l and o, p, respectively. It can be seen that the solder sheared in the liquid nitrogen environment was unable to absorb the deformation and strain energy due to a lack of ductility in the low-temperature environment. The plastic deformation was limited at -196°C; in other words, an increase in the yield strength not only resulted in an increased maximum shear load but also caused a shift in the crack initiation and propagation path to the weakest link in the layered and geometrically affected solder joint configuration to the intermetallic compound layer at the substrate-to-solder interface.

In the -196°C temperature environment, the SAC105 solder is expected to have brittle fracture behavior because the temperature is below its ductile-to-brittle transition temperature. However, instead of having a brittle fracture inside the Sn-based solder joint, all of the full fracture propagation occurred at the substrate-to-solder intermetallic compound interface. This phenomenon can be explained using the diagram in Fig. 10, which is a Yoffee diagram that defines the ductile-to-brittle temperature transition.[20–22] From room temperature toward a low-temperature environment, the SAC105 bulk material shows an increase in yield strength (σ_y), where ductile fracture and plastic deformation occur. Of course, the yield strength can be higher or lower at a given temperature, based on the strain rate; however, in this study, all samples were tested with a single shear speed (100 μm/sec), so the strain rate in this pre-established condition was constant. Competing with the yield strength is the breaking stress (σ_B), which is the stress level at which the Sn bulk material experiences crack initiation and propagation toward full fracture, which is not affected by the temperature and more affected by the allowable crack propagation path. As

described in the diagram, at a relatively high temperature, as indicated by condition A in Fig. 10, if the sample experienced an increased applied stress, the yield strength is reached first, and plastic deformation occurs, resulting in crack propagation with a ductile fracture surface because the crack initiation tip region can plastically deform and a crack can propagate in ductile fracture modes. However, if the temperature is below the cross point of the yield strength and breaking stress, as indicated as condition B in Fig. 10, the breaking stress ($\sigma_{B,\ interface}$) is reached before the applied stress reaches the yield strength ($\sigma_{y,\ Sn\ bulk}$) with increased applied stress at that temperature, resulting in a brittle fracture mode because the crack tip region cannot plastically deform and maintain a sharp crack tip radius.[22] Thus, the cross point of the yield strength and breaking stress at point T defines the ductile-to-brittle transition temperature (DBTT). Based on this explanation using the diagram in Fig. 10, the phenomenon of the fracture location shift in the solder joints for room-temperature and cryogenic temperature shearing can be explained.

The maximum shear strength of SAC105 increased in a low-temperature environment and then even more in the liquid nitrogen environment at −196°C. However, before reaching the breaking stress of the Sn-based SAC105 solder joint, which can cause brittle fracture inside the solder joint, the region near the substrate-to-solder interface with high stress concentrations at the geometrical necking area of the solder joint experienced a sufficient stress level for a breaking stress without allowing any plastic deformation since that region did not reach the yield strength. This stress condition, which was induced by a relatively slow strain rate, ultimately showed a fracture mode, usually observed in high-strain-rate conditions like shock conditions, which induced brittle failure modes. Given that the shear speed in these shear tests was relatively slow at 100 μm/s, the results present the possibility that solder interconnects can undergo full crack propagation similar to that of shock-induced failures but at low strain rates. These results also demonstrate and suggests a need for a new testing approach that couples a low strain rate and a low temperature that can reveal the interconnect mechanical stability and behavior in a cryogenic temperature environment.

CONCLUSION

A simple shear test method to evaluate the solder joint stability of SAC105 solder joints at liquid nitrogen temperature was performed to compare samples with NiAu and Cu-OSP surface finishes. The maximum shear strength of SAC105 solder joints with a NiAu surface finish tested at −196°C decreased with an increase in the aging time at 150°C, with the weak interface found to be the interface between the Ni and (Cu, Ni)$_6$Sn$_5$. Variability in the SAC105 Cu-OSP maximum shear load data was found to be due to the mixed-mode fracture path, which indicated the presence of a weak Cu-OSP interface with transgranular and intergranular fractures inside the Cu_6Sn_5 grains with short aging times; however, the interface shifted to the interface between the Cu_6Sn_5 and solder, resulting in a faster crack propagation path. EBSD analysis on partially sheared solder joints showed that room-temperature shearing induced localized deformation in the SAC105 bulk region at the shear tool contact area, which can absorb the strain energy by plastic deformation. Shearing at −196°C showed restricted plastic deformation compared to that for the room-temperature shearing and resulted in the movement of the full fracture location to the interface between the solder and substrate at the intermetallic compound layers. An increase in the shear strength was observed during shearing at liquid nitrogen temperature compared to that at room temperature due to the brittleness of the solder and reaching the breaking stress ahead of the yield stress. The results present the possibility that solder interconnects can have full crack propagation similar to that of shock-induced failures even at low strain rates. This suggests that a combination of a low strain rate and interconnect mechanical stability in cryogenic temperature environments is critical to understand, which ultimately can help to achieve interconnect reliability in subzero and cryogenic temperature environments.

ACKNOWLEDGMENTS

This work is an outcome of a research collaboration project between Portland State University and Nordson Dage. The authors also want to thank Tony Chen and Greg Baty in the Center of Electron Microscopy and Nanofabrication (CEMN) at Portland State University for their technical support on EBSD imaging and analysis.

CONFLICT OF INTEREST

The authors declare that they have no conflict of interest.

REFERENCES

1. T. Bayer, M. Bittner, B. Buffington, G. Dubos, E. Ferguson, I. Harris, M. Jackson, G. Lee, K. Lewis, J. Kastner, R. Morillo, R. Perez, M. Salami, J. Signorelli, O. Sindiy, B. Smith, M. Soriano, K. Kirby, and N. Laslo, in *IEEE Aerospace Conference proceedings* (Big Sky, MT, US 2019), pp. 1–24.
2. Mission to Europa: Europa Clipper (JPL webpage), https://www.jpl.nasa.gov/missions/europa-clipper/. Accessed 25 August 2020.
3. E. Charbon, F. Sebastiano, A. Vladimirescu, H. Homulle, S. Visser, L. Song, and R.M. Incandela, in *IEEE International Electron Devices Meeting (IEDM) proceedings*, (San Francisco, CA, 2016) pp. 13.5.1–13.5.4.
4. A. Lupinacci, A. Shapiro, J. Suh, and A. Minor, in *IEEE International Symposium on Advanced Packaging Materials proceedings* (2013), pp. 82–88.

5. P. Ratchev, B. Vandevelde, and B. Verlinden, *IEEE Trans. Compon. Packag. Technol.* 30, 416 (2007).
6. Q. An, C. Wang, X. Zhao, and H. Wang, in 18th International Conference on Electronic Packaging Technology proceedings (ICEPT), Harbin, China (2007), pp. 1233–1237.
7. K. Lambrinou, W. Maurisse, P. Limaye, B. Vandevelde, B. Verlinden, and I. Wolf, *J. Electron. Mater.* 38, 1881 (2009).
8. T.-K. Lee, B. Zhou, T. Bieler, and K.-C. Liu, *J. Electron. Mater.* 41, 273 (2012).
9. T.-K. Lee, C.-U. Kim, and T. Bieler, *J. Electron. Mater.* 43, 69 (2014).
10. T.-K. Lee, C.-U. Kim, and T. Bieler, *J. Electron. Mater.* 45, 171 (2016).
11. R. Tian, Y. Tian, C. Wang, and L. Zhao, *Mat. Sci. Eng. A* 684, 697 (2017).
12. P. Ratchev, T. Loccufier, B. Vandevelde, B. Verlinden, S. Teliszewski, D. Werkhoven, and B. Allaert, in IMAPS Eur. Microelectron. Pack. Conf. proceedings, Brugge, Belgium (2005), pp. 248–252.
13. C. Tseng, T.-K. Lee, G. Ramakrishna, K. Liu, and J. Duh, *Mater. Lett.* 65, 3216 (2011).
14. S. Fu, C. Yu, T. Lee, K. Liu, and J. Duh, *Mater. Lett.* 80, 103 (2012).
15. F. Gao and T. Takemoto, *Mater. Lett.* 60, 2315 (2006).
16. D. Mu, H. Huang, and K. Nogita, *Mater. Lett.* 86, 46 (2012).
17. J. Xian, Z. Ma, S. Belyakov, M. Ollivier, and C. Gourlay, *Acta Mater.* 123, 404 (2017).
18. G. Zeng, S. McDonald, J. Read, Q. Gu, and K. Nogita, *Acta Mater.* 69, 135 (2014).
19. S. Wright, N. Nowell, and D. Field, *Microsc. Microanal.* 17, 316 (2011).
20. S. Jin, W. Horwood, J.W. Morris Jr, and V. Zackay, *Adv. Cryog. Eng.* 19, 373 (1995).
21. J.W. Morris Jr, C. Lee, and Z. Guo, *ISIJ Int.* 43, 410 (2003).
22. J.W. Morris Jr, *Science* 320, 1022 (2008).

Publisher's Note Springer Nature remains neutral with regard to jurisdictional claims in published maps and institutional affiliations.